A&A 506, 1405–1414 (2009)
DOI: 10.1051/0004-6361/200912441

Astronomy & Astrophysics

Solar granulation from photosphere to low chromosphere observed in Ba II 4554 Å line

R. Kostik[1], E. Khomenko[2,1], and N. Shchukina[1]

[1] Main Astronomical Observatory, NAS, 03680 Kyiv, Ukraine
e-mail: kostik@mao.kiev.ua
[2] Instituto de Astrofísica de Canarias, 38205 La Laguna, Tenerife, Spain

Received 7 May 2009 / Accepted 10 August 2009

ABSTRACT

Aims. The purpose of this paper is to characterize the statistical properties of solar granulation in the photosphere and low chromosphere up to 650 km.

Methods. We use velocity and intensity variations obtained at different atmospheric heights from observations in Ba II 4554 Å. The observations were done during good seeing conditions at the VTT at the Observatorio del Teide on Tenerife. The line core forms rather high in the atmosphere and allows granulation properties to be studied at heights that have been not accessed before in similar studies. In addition, we analyze the synthetic profiles of the Ba II 4554 Å line by the same method computed taking NLTE effects into account in the 3D hydrodynamical model atmosphere.

Results. We suggest a 16-column model of solar granulation depending on the direction of motion and on the intensity contrast measured in the continuum and in the uppermost layer. We calculate the heights of intensity contrast sign reversal and velocity sign reversal. We show that both parameters depend strongly on the granulation velocity and intensity at the bottom photosphere. The larger the two parameters, the higher the reversal takes place in the atmosphere. On average, this happens at about 200–300 km. We suggest that this number also depends on the line depth of the spectral line used in observations. Despite the intensity and velocity reversal, about 40% of the column structure of granulation is preserved up to heights around 650 km.

Key words. Sun: photosphere – Sun: chromosphere – Sun: granulation – techniques: spectroscopic – radiative transfer

1. Introduction

Convective motions in the solar atmosphere have been studied in detail during the past decades, using different types of observations, their analysis, and interpretation. The summary of the investigations before 2000 can be found in Espagnet et al. (1995) and Brandt (2000). According to the final results, the photosphere can be divided into two regions with different physical properties with the border between them lying at heights about 170 km above the continuum formation height (see Espagnet et al. 1995, for details). This conclusion was reached based on the amplitudes of intensity and velocity fluctuations first decreasing with height, reaching minimum at about 170 km and then starting to increase again. The intensities and velocities at heights above and below 170 km do not seem to be correlated with each other. On the other hand, Espagnet et al. (1995) came to the conclusion, based on their own investigations, that the photosphere can be divided into these two regions only in intensity fluctuations, since the vertical convective velocity structure is preserved until heights as high as 500 km. A similar result has also been obtained by Salucci et al. (1994).

During the past few years significant efforts have been made to determine the precise height where the inversion of intensity contrast (or temperature) takes place. The results by different authors diverge significantly in this respect. Values as low as 60 km are found by Kneer et al. (1980) from spectrograms of the Mg I b_2 line taken at the quiet Sun disk center. While Bendlin & Volkmer (1993) give values as high as 270 km from 2D spectral images obtained with tuning a Fabry-Perot interferometer in the Fe I 6303 Å line in a moderately active region near disk center. Different values are also given in the more recent literature, e.g. 250 km (Kostyk & Shchukina 2004), 200 km (Janssen & Gauzzi 2006), 170 km Puschmann et al. (2005). In the last paper, the authors perform a careful analysis and NLTE inversion of the observed spectral profiles of the several photospheric Fe I lines and present the resulting temperature and velocity stratifications as functions of both optical depth and geometrical height. In addition to the height of inversion of the intensity contrast (temperature), they also report that only the large-scale structures (about 4″) penetrate to higher layers without the lost of correlation though the whole atmosphere. Similar results were also reported by Puschmann et al. (2003), where the authors find that only the intensity structures with sizes over 2″ at heights about 435 km are still connected with those at the continuum level.

In all the papers reported above (except Kostyk & Shchukina 2004), the vertical velocities were observed in phase though the whole photosphere penetrating into the highest layers under study. Only Kostyk & Shchukina (2004) have obtained evidence of the velocity reversal at heights above 490 km for the elements with the highest contrast in their data (above 6–9%).

The spectral lines used in previous studies gave the possibility of analyzing statistical properties of solar granulation mainly in photospheric layers below the temperature minimum. The aim of the present paper is to extend this analysis to the higher layers taking advantage of spectral observations in the Ba II 4554 Å line. According to Olshevsky et al. (2008) and Sütterlin et al. (2001), the core of this line forms rather high at about 700 km. It makes the line particularly useful for studying the vertical

structure of the solar atmosphere, since we can follow this structure to much greater heights than in the previous analysis. Recent theoretical investigation (Shchukina et al. 2009, hereafter referred to as Paper I) based on NLTE modeling the Ba II 4554 Å line in a three-dimensional (3D) hydrodynamical model have shown that this line is a valuable tool for the Doppler diagnostics along the whole photosphere and lower chromosphere.

In the present study we use theoretical understanding attained in Paper I for interpreting the new high-resolution spectral observations in the Ba II 4554 Å line. We investigate the column structure of granulation up to the heights above the solar temperature minimum, derive the height of the intensity contrast sign reversal and the change of sign of the vertical motions, and propose a 16-column model of granulation, depending on the direction of motion and intensity in the low and high photospheres. The results of observations are compared with the NLTE calculations of the Ba II 4554 Å line profiles in the 3D HD model of solar convection by Asplund et al. (2000).

2. Observations

Observations were obtained in July 21, 2004 at the 70-cm German Vacuum Tower Telescope (VTT, see Schröter et al. 1985, for description) at the Observatorio del Teide in Tenerife during the good seeing conditions. The observations were done with Echelle spectrograph. The spectral region was centered on the Ba II 4554 Å line. Using the narrow-band Ca II K and Hα slit-jaw images, we selected a quiet region free of magnetic activity close to the solar disk center. Spectral images were recorded with a CCD camera with 1024 by 1024 pixels. The size of the images in spectral direction was 4.1 Å. The width of the spectrograph entrance slit was 100 μm (equivalent to 0.″46). One pixel corresponds to 0.″087 on the solar surface. This way, the field of view of the telescope was 0.″46 by 89″. However, after the reduction, only about 730 pixels were found to be useful for the analysis, equivalent to the 63.″5 of the solar surface. The time series of Ba II 4554 spectral images was obtained with a fixed slit position of the total duration of 69.9 min with an interval of 7 s. The exposure time was 1 s, and a total of 600 exposures were taken. The image of the observed area was stabilized using the adaptive optics (AO) system guiding on solar granulation. The average Fried's parameter, as given by AO, was fluctuating around R_0 = 7–8. The spatial resolution of observations limited by the image motion on the spectrograph slit due to earth atmospheric turbulence was estimated to be about 0.″3–0.″7.

3. Reduction of observations and calculation of line parameters

Following the standard procedure, all 600 spectral images were reduced for flatfield (e.g. Kiselman 1994). The flat field images were recorded immediately after the time series of Ba II spectra in the same wavelength at the solar disk center. The spatial structure of the solar surface was removed from the flatfield images by rapid motions of the telescope scan mirror. The reduction for flatfield included the following steps:

- removing the dark current out of the spectral images and the flatfield images;
- correction of all the images for the inclination and distortion of the spectrograph sit with respect to the pixel direction of the CCD;
- removing the solar spectral lines from flatfield images;
- splitting the flatfield images into the two components. Here we need additional explanations. Both CCD camera and the spectrograph slit have some dust on them. The dust at the CCD camera appears as dark dots on the spectral images, while the dust at the slit appears as dark horizontal lines, similar to intergranular lanes. As the dust position on the slit can change with time, the position of these dark lines on the spectral images and on the flatfield images is not always the same. Thus, we had to split the flatfield images into the images containing only a CCD dust component (matrix flatfield) and those containing only the slit dust component (slit flatfield);
- removing the matrix flatfield from spectral images. This can be done automatically. Removing the slit flatfield requires individual control of all the spectral images, since the positions of the dark lines do not always coincide. In some cases we had to recalculate the slit flatfield images by shifting them in a spatial direction by a fraction of a pixel.

The next step in the data reduction included calculating of the intensity and velocity variations at different positions of the Ba II line profiles. For that we used a λ-meter technique. The description of this method can be found in Stebbins & Goode (1987) and Shchukina et al. (2009, Paper I).

We used 55 reference widths of the average Ba II 4554 Å line intensity profile $\Delta\lambda_W = \overline{\Delta\lambda_\mathrm{r}} - \overline{\Delta\lambda_\mathrm{b}}$, where $\overline{\Delta\lambda_\mathrm{r}}$ and $\overline{\Delta\lambda_\mathrm{b}}$ are the wavelengths of the red and blue wings, respectively. For each individual Ba II profile at each spatial position x (varying from 1 to 730) and time moment t (varying from 1 to 600), we then found intensity variations $\delta I(t, x, W)$ and velocities $V(t, x, W)$ at the corresponding 55 reference widths. We slightly modified the standard λ-meter procedure as described below, keeping in mind that the formation heights of the blue and red wing intensity points of the line profile are, in general, not the same because of the Doppler velocity shift (see e.g. Shchukina et al. 2009, Paper I). The velocities were calculated separately in the red and blue wings of the Ba II line in the following way:

$$\begin{aligned} V_\mathrm{r}(t, x, W) &= \delta V_\mathrm{r}(t, x, W) + \bar{V}(W) \\ V_\mathrm{b}(t, x, W) &= \delta V_\mathrm{b}(t, x, W) + \bar{V}(W) \end{aligned} \quad (1)$$

where

$$\begin{aligned} \delta V_\mathrm{r}(t, x, W) &= (c/\lambda) \cdot \delta\lambda_\mathrm{r} \\ \delta V_\mathrm{b}(t, x, W) &= (c/\lambda) \cdot \delta\lambda_\mathrm{b}. \end{aligned} \quad (2)$$

In these equations, $\bar{V}(W)$ is the bisector of average profile due to to nonthermal velocity field

$$\bar{V}(W) = (c/\lambda) \cdot (\overline{\Delta\lambda_\mathrm{r}} + \overline{\Delta\lambda_\mathrm{b}})/2 - V_\mathrm{HFSI}, \quad (3)$$

where V_HFSI is the line bisector caused by the hyperfine structure (HFS) and isotopic shift, c velocity of light and, λ the line wavelength. Furthermore, in Eq. (2) $\delta\lambda_\mathrm{b,r} = \Delta\lambda_\mathrm{b,r} - \overline{\Delta\lambda_\mathrm{b,r}}$ denotes the wavelength shift of the blue (red) intensity point belonging to a certain spectral width relative to the corresponding blue (red) point of the average profile.

We derived the bisector V_HFSI using the Ba II 4554 Å line profile calculated in the MACKKL model (see e.g. Shchukina et al. 2009, Paper I). Figure 1 shows that the bisector V_HFSI is negative (between −0.3 and −0.2 km s^{-1}), while the nonthermal velocity bisector $\bar{V}(W)$ of the average observed profile changes sign ranging from −0.1 km s^{-1} to ≈0.25 km s^{-1}. The velocity values were corrected for the displacement due to the Earth rotation and revolution. Note that through this paper negative velocities

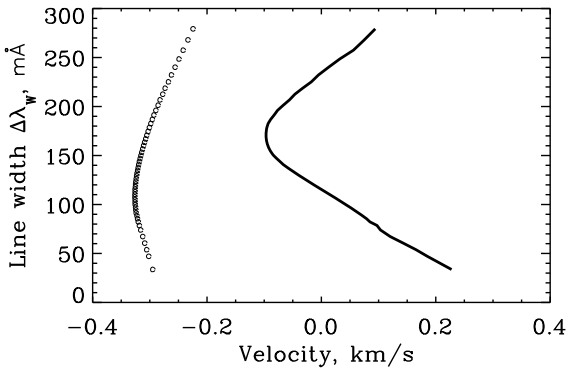

Fig. 1. Bisector due to hyperfine and isotopic shift calculated in the MACKKL model (Maltby et al. 1986) (small open circles), and bisector of the observed profile, average over space and time, caused by the nonthermal velocity field (solid line).

mean downflows and positive velocities mean upflows. The only exception is Fig. 1 where, in agreement with Fig. 2 of Paper I, we assume negative velocity direction to be toward the observer, corresponding to an upflow.

In a similar way, we calculated intensity variations (contrast) $\delta I(t, x, W)$ relative to the intensity $\bar{I}(W)$ of the Ba II line profile averaged over space and time:

$$\delta I(t, x, W) = (I(t, x, W) - \bar{I}(W))/\bar{I}(W). \quad (4)$$

A through analysis of the Doppler diagnostic techniques by Shchukina et al. (2009, Paper I) has shown that the V_b and V_r velocities calculated from the line profile of the Ba II 4554 Å line are, in fact, very close to each other. According to their analysis, both V_b and V_r correspond better to heights of formation H_b of the blue wing intensities, rather than to H_r of the red wing intensities. Guided by the results of Paper I we use the average values $V = (V_b + V_r)/2$ throughout the present paper and ascribe their origin to the average heights of formation of the blue wing intensities.

Variations of intensity $\delta I(t, x, W)$ and velocities $V_r(t, x, W)$ and $V_b(t, x, W)$ are mainly caused by oscillatory and convective motions. By convective motions we mean the motions of individual granules and intergranular lanes. To separate oscillatory and convective components we performed filtering in the Fourier domain based on the diagnostic $k-\omega$ diagram. According to this diagram, we limited the wave motions in temporal frequency between $\omega = 1.8$ and 5.7 mHz and convective motions by frequencies below $\omega = 2.2$ mHz. Additional filtering was performed for convective motions in the spatial frequency, leaving only variations with k less than 0.18 Mm^{-1}. Similar filtering was applied in Khomenko et al. (2001) and Kostik & Khomenko (2007). As the frequency domains overlap, the wave motions can, in principle, contribute to convective motions. The maximum contribution of the wave motions at $\omega = 3.3$ mHz reaches 4.2%. We checked that decreasing this contribution to 3.1% (more narrow filter) or increasing it to 20% (more wide filter) produces only an insignificant influence on our results. As an example we show in Fig. 2 the convective (left) and oscillatory (right) components of the velocity corresponding to heights around 650 km as a function of space and time. The vertical axis represents the velocity amplitudes. The different temporal and spatial behavior of the both components is evident from the figure. In the rest of the paper we focus our analysis on the convective component of the velocity and intensity variations. In addition, we only select a part of the time series (of about 200 exposures) when the seeing conditions were the best; i.e., the estimated spatial resolution was not worse than 0.″4.

4. Formation heights along the observed Ba II line profiles

The formation heights of the 55 reference widths of the Ba II 4554 Å intensity profiles were obtained from NLTE calculations in a 3D hydrodynamic model atmosphere by (Asplund et al. 2000). Detailed description of the Barium atomic model, NLTE calculations, and the 3D hydrodynamical snapshot is given in Olshevsky et al. (2008) and Shchukina et al. (2009, Paper I). In this section we present additional information that can be useful for understanding our results.

Figure 3 visualizes vertical variations in the velocity along one of the slices of this snapshot. The geometrical height is the same in all the points of the snapshot, but the optical depth scale is fluctuating from column to column due to horizontal inhomogeneities of the thermodynamic quantities. The zero point of geometrical height $H = 0$ is assigned by averaging over all grid points of the snapshot the locations where the continuum optical depth $\tau_{5000} = 1$ (see Asplund et al. 2000).

The vertical extent of the snapshot was optimized to reach high enough layers (till 900 km) to allow reliable calculation of the cores of strong lines (see Asplund et al. 2000; Stein & Nordlund 1998; Nordlund & Dravins 1990). Taking into account that the core of the Ba II 4554 Å line is formed more than 100 km below the upper boundary (Shchukina et al. 2009, Paper I), one can expect the effects of the upper boundary conditions to be negligible for spectral synthesis of this line. An excellent agreement of the spatially average synthetic profile and observed profile from the Liége atlas (Delbouille et al. 1973), as well as profile obtained from observations at the VTT, supports this conclusion (see Fig. 4 in Shchukina et al. 2009, Paper I).

The solar disk-center profiles of the Ba II 4554 Å line were calculated by means of 1D multilevel NLTE radiative transfer employing a set 1D models from individual grid points of the 3D snapshot as input. Such an approach is known in the literature as 1.5D approximation.

For each grid point (1D model), we calculated formation heights of the blue wing intensities H_b corresponding to 55 reference widths $\Delta\lambda_W$ of the Ba II profile. Following Shchukina et al. (2009, Paper I), we used the concept of Eddington-Barbier heights of line formation; i.e., we evaluated heights where the line optical depth at a given wavelength point $\Delta\lambda$ is equal to unity: $\tau(\Delta\lambda) = 1$. We then assumed that the information on vertical velocity and intensity at wavelength point $\Delta\lambda$ comes from this height. We repeated the calculations of H_b heights for all grid points of the 3D snapshot and then computed an average value $\langle H \rangle$ for each of the 55 reference widths $\Delta\lambda_W$. These formation heights were ascribed to the corresponding widths of the observed intensity profiles. Thus, the formation heights calculated this way are model-dependent.

According to Shchukina et al. (2009, Paper I), the mean formation heights $\langle H \rangle$ of each section of the Ba II 4554 Å line profile have a well-pronounced dependence on the spectral width of this section. Thus, the intensity and velocity information coming from each width level $\Delta\lambda_W$ of the observed profile roughly corresponds to a different height in the atmosphere. The selected widths $\Delta\lambda_W$ of observed profiles vary between 280 mÅ and 30 mÅ. The corresponding range of the mean formation heights lies between ∼−25 km and ∼650 km.

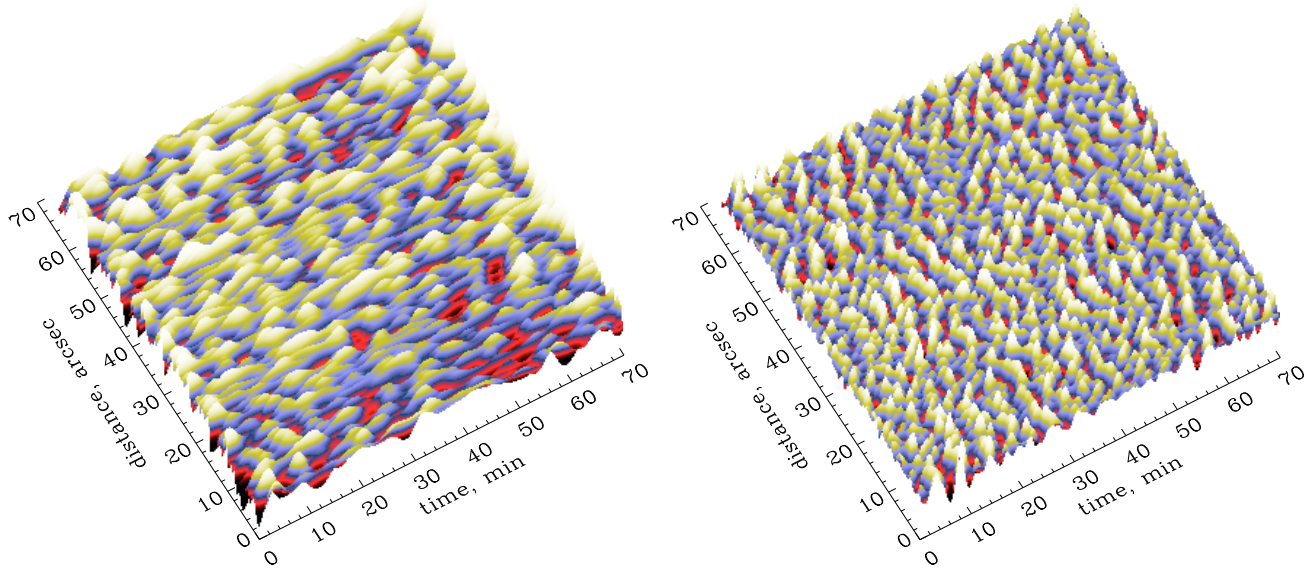

Fig. 2. Convective (*left panel*) and oscillatory (*right panel*) components of the velocity field corresponding to heights about 650 km as a function of the slit position and time.

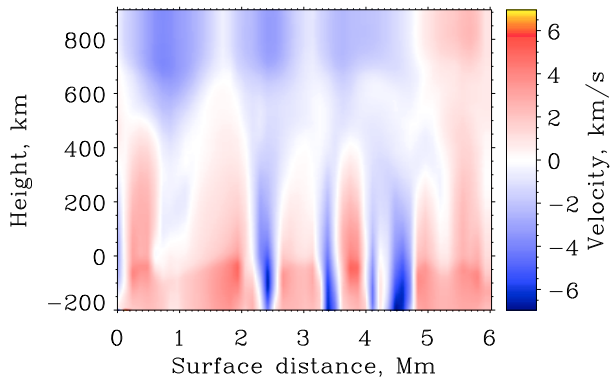

Fig. 3. Vertical velocities along one of the slices in the 3D model. Negative velocities correspond to intergranules (downflow, blue color), while positive velocities correspond to granules (upflow, red color).

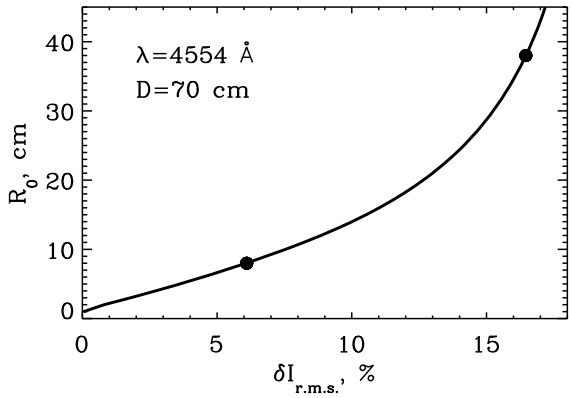

Fig. 4. Root-mean-square continuum contrast $\delta I_{\rm rms}$ as a function of Fried's parameter R_0 for wavelength λ = 4554 Å and for telescope diameter D = 70 cm. The $\delta I_{\rm rms}$ curve was calculated using 3D radiative transfer formal solution for continuum intensity obtained by Trujillo Bueno & Shchukina (2009) in the 3D HD model. Filled circles correspond R_0 = 8 cm ($\delta I_{\rm rms}$ = 6.1%) and R_0 = 38 cm ($\delta I_{\rm rms}$ = 16.5%).

The lowest height level corresponds to the width $\Delta\lambda_W$ = 280 mÅ, and its average formation height is $\langle H\rangle = -25$ km. We used the intensity variations at this level as a criterion for separating granular and intergranular regions. Taking into account that this height is expected to be close to the formation height of the continuum intensity, we call "granules" those features whose intensity $I(t, x, W)$ at $\Delta\lambda_W$ = 280 mÅ ($\langle H\rangle = -25$ km) was larger than the average $\bar{I}(W)$. The classical definition of "granule" and "intergranule" can only be applied to the continuum formation heights. Higher in the atmosphere, this definition does not make sense.

4.1. Spatial smearing and determination of Fried's parameter

To directly compare between the synthetic and observed spectra, we performed a convolution of the synthetic profiles with a corresponding modulation transfer function (MTF) representing the action of the 70-cm telescope and Earth's atmosphere (see e.g. Khomenko et al. 2005; Shchukina et al. 2009). In such an interpretation the quality of the resulting image depends on the telescope diameter D and Fried's parameter R_0 (Fried 1966). To perform the smearing, the original 2D intensity maps at each individual wavelength were Fourier-transformed and multiplied by MTF calculated for known telescope diameter (70 cm, VTT) and Fried's parameter R_0. The corresponding MTFs are given in Shchukina et al. (2009). An inverse Fourier transform was performed to obtain the smeared images, i.e., the images affected by the diffraction on the telescope aperture and the seeing effects.

Ricort et al. (1981) proposed determining R_0 from the observed rms continuum contrast of solar granulation $\delta I_{\rm rms}$. Following their idea, Shchukina et al. (2009) calculated theoretical dependences between $\delta I_{\rm rms}$ and the Fried's parameter R_0 at different wavelengths. These authors used 3D radiative transfer solution for the solar continuum intensity obtained by Trujillo Bueno & Shchukina (2009) in the same snapshot of the 3D HD model. We applied their theoretical calibration curve at wavelength λ = 4554 Å to define Fried's parameter R_0 from our observations (see Fig. 4). We found that, with the spatial resolution reached during the observations (~0.″7–0.″3), the root-mean-square continuum contrast $\delta I_{\rm rms}$ at the wavelength of the

Ba II line is between 5.4% and 6.3%. Thus, we estimate Fried's parameter R_0 in the range between 7 cm and 8 cm.

5. Results of observations and comparison with model calculations

According to Shchukina et al. (2009, Paper I), the λ-meter technique applied to the Ba II 4554 Å line profiles recovers velocities at different heights rather well. Nevertheless, there are three important points that we have to keep in mind.

First, under seeing conditions corresponding to our observations, (R_0 = 7–8 cm) the velocities derived from the inner wings ($\Delta\lambda_W$ < 150 mÅ) of the Ba II 4554 Å line profiles are more reliable than from the outer wings (see Paper I, Fig. 9). In the former case, the correlation coefficient between the original and λ-meter velocities varies between 0.7–0.8, while in the latter it becomes lower (about 0.6).

Second, such a parameter as the average formation height should be used with caution. In reality, the intensities corresponding to a single value of $\Delta\lambda_W$ are formed in a wide range of heights, depending on the model atmosphere. The peak-to-peak formation height variations can be as much as 200 km in the outer blue wings and even more (~500 km) in the inner blue wings (see Paper I, Fig. 13).

Third, the absolute values of the λ-meter velocities are lower than the original ones. This is not surprising. On the one hand, we recover velocities from the synthetic profiles degraded by atmospheric seeing. This should lower the absolute values of the velocities. On the other hand, the λ-meter technique itself leads to smoothing and vertical averaging of the velocities within the heights where the line intensity is formed.

Taking these limitations into account, we discuss below in this section the results of application of λ-meter technique to our observations. Kostyk & Shchukina (2004) have shown that the granular motions in the lower photosphere preserve their column structure up to height of 490 km. We can verify this result because the Ba II line allows us to investigate the properties of the granulation at greater heights up to 650 km. Using 200 spectral images taken during the best seeing conditions of the series, we calculated the number of "convective columns" at each of 55 $\Delta\lambda_W$ positions. This number was defined as a number of contrast sign changes (or, independently, the velocity sign changes) along the slit at each height. We normalize the number of these columns (independently for velocity and intensity) to the total number at the lowest layer. The results are presented in Fig. 5. The horizontal axis of the both panels of this figure gives the average NLTE formation heights corresponding to 55 values of the profile widths $\Delta\lambda_W$. The vertical axis of the top panel gives the percentage of the locations of intensity contrast (squares) and the velocity direction (triangles) changes along the surface, calculated with respect to the lowest layer. The bottom panel of the figure gives similar information but averaged over the velocity and intensity. As expected, the number of the locations where the contrast sign or the direction of motion changes decreases with height, both for velocity and intensity events (top panel of Fig. 5). There are about 20% fewer events for intensity at all heights. However, an unexpected result (at least for us) was that about a half of the convective structures (40%) registered in the continuum are maintained with height as high as at 650 km.

Next we investigated how the size of the convective structures changes with height. We define the size as a simple difference in spatial coordinate between the successive changes in the sign of the contrast or in sign of the velocity. The results are shown in Fig. 6. The horizontal axis of the figure gives the size of the convective structures, and the vertical axis gives the fraction of the structures of a given size in percent. The curves are normalized to the corresponding number of elements found at the lowest layer from the velocity variations. The upper curves

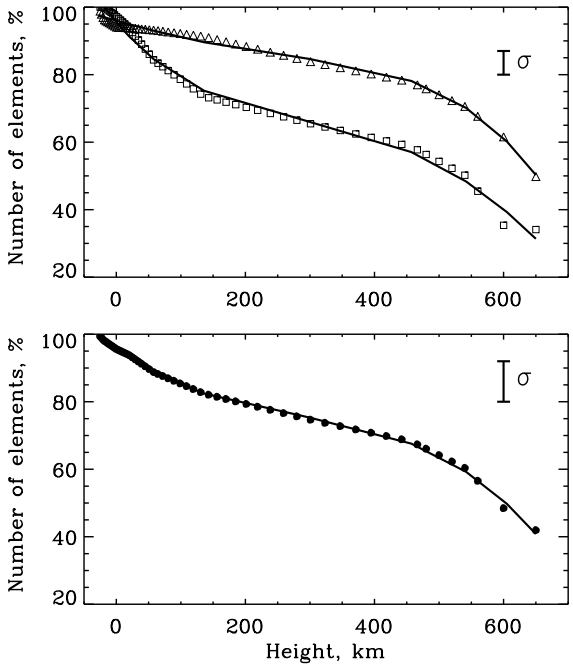

Fig. 5. *Top*: fraction of the spatial locations where the intensity contrast sign (squares) and the velocity direction (triangles) at a given height (or $\Delta\lambda_W$) changes along the slit. *Bottom*: same, but averaged over the velocity and intensity events.

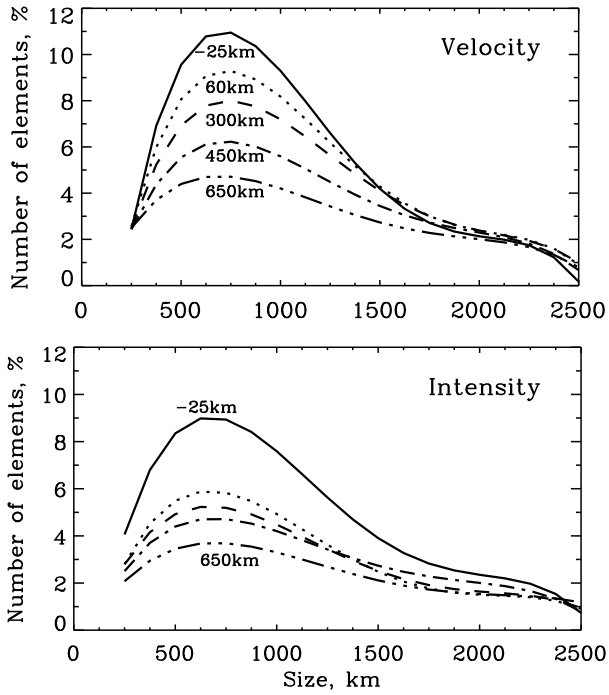

Fig. 6. The fraction of the convective structures with a given size at different heights in the atmosphere. The curves (from the upper to the lower) correspond to average heights $\langle H\rangle$ = −25, 60, 300, 450, and 650 km. Top panel: size calculated from the velocity variations; bottom panel: size calculated from the intensity variations.

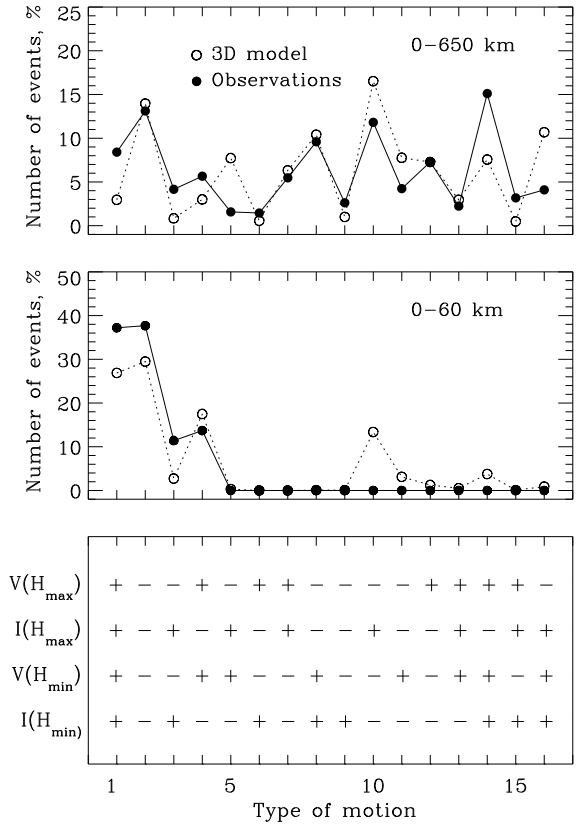

Fig. 7. Convective motions in the solar atmosphere according to 16-column model. *Upper panel* shows the number of cases corresponding to each of the 16 types of motions (as defined at the *bottom panel*) between 0 and 650 km. *Middle panel* gives the same but for heights between 0 and 60 km. Solid line: observations. Dotted line: 3D HD model.

in both panels in Fig. 6 correspond to the average height of $\langle H \rangle = -25$ km and the lower curves to the height of 650 km. The maximum of both velocity and intensity distributions appears at 650–700 km granular size. The number of structures with this size decreases with height from about 11% at −25 km to ∼4% at 650 km (as defined by velocity variations) and from ∼9% to ∼3% (as defined by the intensity variations). Convective structures that have larger sizes (about 1500–1700 km) at the height of continuum formation almost always reach the upper layers. Their fraction with height is almost constant. It means that the average size of convective elements gets larger with height. Here we need to give additional explanations. We did not follow the behavior of each individual structure with height. It means that, most probably, not all the large-size convective structures with sizes above 1500 km at $\langle H \rangle = -25$ km reach a height of 650 km. It can instead be a result of merging of the convective structures with smaller sizes. In either case, we can conclude that, in the height range 0–650 km in the solar atmosphere, the fraction of the convective structures with sizes 1500–2500 km is almost constant.

How do individual properties of the convective elements change with height? We assume that the convective elements observed at the uppermost layer at 650 km can either preserve their contrast and velocity direction from the continuum formation height or change them by the opposite. This way we define 16 types of motion. These types of motion are outlined in the lower panel of Fig. 7. The "+" sign stands for convective elements moving upwards or those whose contrast is above the average. The "−" sign stands for those elements moving downwards or having the contrast below the average. All 16 types of motions are indeed present in the solar atmosphere. The upper panel of Fig. 7 gives the number of cases corresponding to each of the 16 types of motion between 0 and 650 km heights, in percent (solid line). The number of cases changes from the lowest value of 1.4% (case number 6; downward moving hot material in the continuum and upward-moving cold material at 650 km) to the highest value of 15.1% (case number 14; upward-moving hot material in the continuum and upward-moving cold material at 650 km). Only 21.4% of the elements show the pure convective character of motion (i.e. hot material rises, cold material sinks). The latter number contains the sum of the cases 1 and 2 (8.3 + 13.1). This number can be even lower if the convective motions change their direction of motion or sign of contrast several times between 0 and 650 km. In contrast, in some 9.9% of the cases, the cold material rises and the hot material sinks (cases 3 and 4). The remaining 68.7% of the convective elements either change their sign of contrast (31.7%) or direction of motion (18.8%) or both (18.2%) between 0 and 650 km.

The middle panel of Fig. 7 gives the properties of the convective motions in the low photosphere close to the continuum formation level (solid line) between 0 and 60 km. Most of the convective elements preserve their properties within this low height range. However, even in this case only 75% of the elements follow the classical convection behavior, while about 15% of the relatively cold material moves upwards and 10% of the relatively hot material moves downwards.

Similar analysis was also performed with synthetic line profiles (see dotted curves in the upper and middle panels of Fig. 7). It is evident that the 3D hydrodynamical model of Asplund et al. (2000) describes many properties of the observed variations in intensity and velocity, both qualitatively and quantitatively. Only the case of motion number 10 has a highest percentage in the simulations (15%) at heights 0–60 km compared to its absence in the observations (middle panel).

The results shown in Fig. 7 are unlikely to be produced by noise in the observations or the influence of the upper boundary conditions in the simulations. By applying the filter to separate the wave and the convective motions, the high-frequency noise component is completely excluded from the observed variations. As for the simulations, the Ba II line is formed about 100 below the upper boundary of the simulation domain, so its influence should be negligible.

According to the conclusions derived from Fig. 7, the convective elements not only change their sign of contrast with height but also change the direction of the velocity. The latter property has not received much attention in the literature, except the work of Kostyk & Shchukina (2004). What are the typical heights where the sign reversal of the convective intensity and velocity takes place? From the first look at our observations, we find that there is a big scatter in such heights, from 50 to 650 km. However, we find that the cause of such a big scatter is not in systematic or random errors. This scatter comes from the intrinsic properties of convective elements, i.e. their contrast and velocity. This conclusion is illustrated in Figs. 8 and 9 for observations with the best rms continuum contrast $\delta I_{\rm rms} \approx 6\%$ (solid curves with filled circles). The solid curve in the left panel of Fig. 8 shows that the height of the velocity sign reversal depends on the strength of the granular velocities at the lowest level[1]. The

[1] As discussed in Sect. 4, the heights are defined with respect to the average location of $\tau_{5000} = 1$ over all grid points of the 3D snapshot. The velocities and intensities at $\langle H \rangle = -25$, as given on the horizontal axis of Figs. 8 and 9, are measured from the observed profiles at $\Delta\lambda_W \sim 280$.

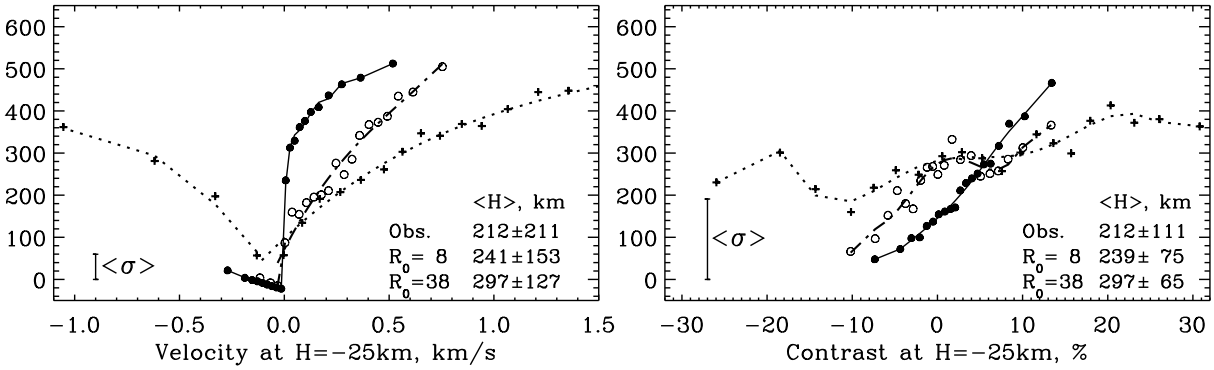

Fig. 8. Height of the velocity sign reversal as a function of the velocity (*left*) and contrast (*right*) at the average height $\langle H \rangle = -25$ km. Thick solid lines with filled circles result from observations, dash-dotted lines with open circles and dotted lines with crosses result from synthetic profiles convolved with an MTF function representing the action of the 70-cm telescope and the Earth atmospheric turbulence with Fried's parameters $R_0 = 8$ cm and $R_0 = 38$ cm, respectively. Each symbol is an average over bin with an equal number of data points. Standard deviation $\langle \sigma \rangle$ averaged over all bins is shown in each panel. The mean heights of the velocity sign reversal are given in the lower right corner.

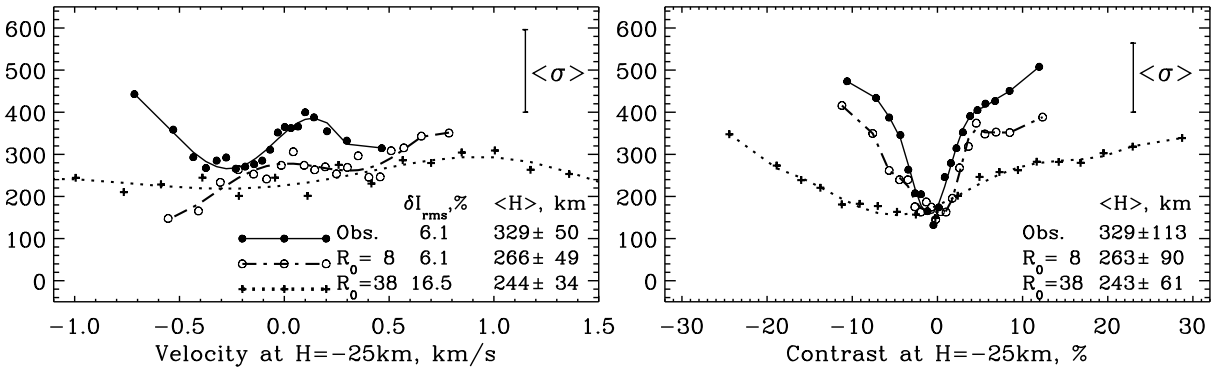

Fig. 9. Height of the contrast sign reversal as a function of the velocity (*left*) and contrast (*right*) at the average height $\langle H \rangle = -25$ km. The format of the figure is the same for as Fig. 8.

higher is the velocity of granules, the higher in the atmosphere the velocity sign reversal takes place. The curve is asymmetric with respect to zero velocity value. Given the same absolute value of the velocity, the downward-moving convective elements change their sign of velocity at substantially lower heights than the upward moving elements. The average value of the height of the velocity sign reversal is 212 ± 211 km.

The right panel of Fig. 8 gives the velocity sign reversal height as a function of contrast corresponding the most bottom layer ($\langle H \rangle = -25$ km). Similar to the above, the higher the contrast of granules in the continuum, the greater the height of the velocity sign reversal. There is again an asymmetry in the granulation properties. The bright granules change their sign of velocity at much greater heights than the dark intergranular lanes. The difference can be as much as 300 km for the features with the continuum contrast of ±7.5%.

Figure 9 illustrates the dependence of the height of contrast sign reversal on the velocity (left panel) and intensity (right panel) at $\langle H \rangle = -25$ km. The left panel of this figure shows that, the lower the downward convective velocity at bottom level, the greater the height of the contrast sign reversal of these elements. This is what expected considering that the observed correlation between convective velocity and intensity in the deep photospheric layers is rather high (e.g. Kostyk & Shchukina 2004). On average, the contrast sign reversal takes place at $\langle H \rangle = 329 \pm 50$ km, which is higher than the velocity sign reversal by ∼100 km. According to the right panel of Fig. 9, the contrast sign reversal occurs approximately at the same height both for granules and intergranules, as defined by their continuum intensity. The higher the absolute value of the continuum intensity, the higher the reversal occurs in the atmosphere.

In general, the agreement between the observed dependences and the synthetic ones calculated for the same seeing ($R_0 = 8$ cm) is fairy satisfactory. However, the agreement is worse for results presented in the left panel of Fig. 9, where the contrast sign reversal height of the elements with downward granular velocities calculated from 3D model are considerably lower. The reason for that lies in the poor correlation between the velocity and contrast at the bottom layer $\langle H \rangle = -25$ km of the 3D model. In the 3D model, the correlation coefficient is rather low (∼0.35), while it is appreciably higher, (∼0.65) in observations. These values of the correlation coefficients agree with the results obtained earlier from three iron lines by Kostyk & Shchukina (2004).

Figure 10 gives additional illustration of the granular velocity and intensity behavior with height. It shows several examples of the observed horizontal variations of the contrast (left) and velocity (right) along the solar surface at different heights. The curves demonstrate clearly that the amplitudes of the variations becomes progressively weaker with height and the sign reversal takes place. Such a reversal is especially evident at spatial locations around 1.5, 3, and 5 Mm.

The dependences discussed above from Figs. 8–10 were obtained from the ground-based observations under good seeing

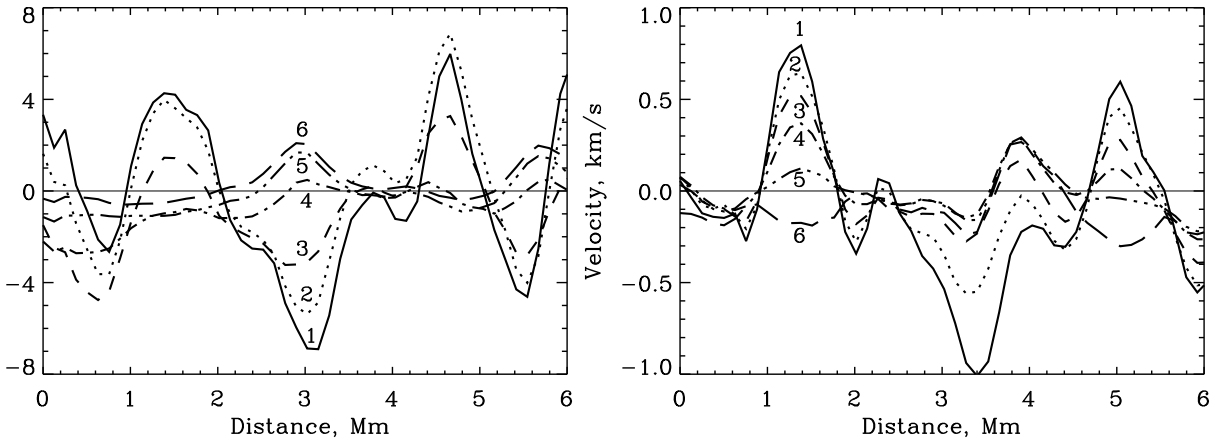

Fig. 10. *Left*: observed variations of the granulation contrast along the solar surface at several heights. The curves numbered from 1 to 6 correspond to the average heights: $\langle H \rangle$ = 0, 60, 300, 450, 600, and 650 km. *Right*: same for the velocities.

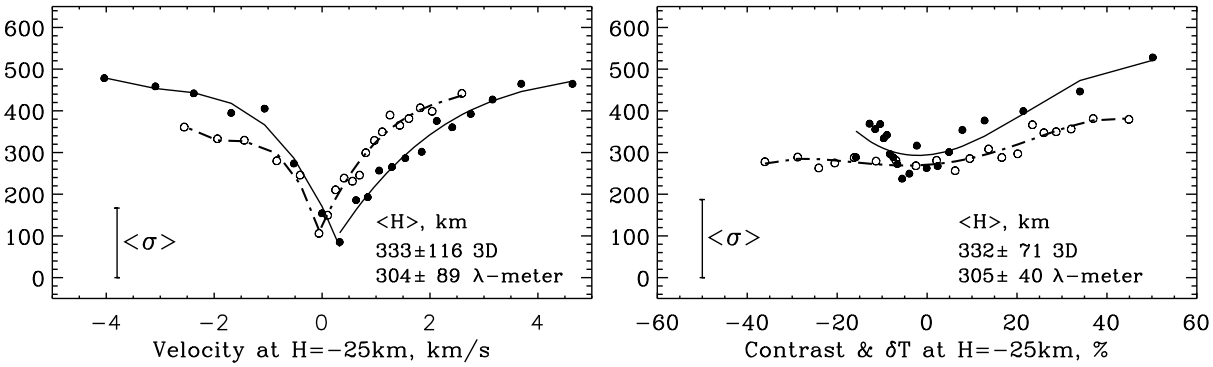

Fig. 11. Height of the velocity sign reversal as a function of the velocity (*left*) and as a function of contrast or temperature variations δT (*right*) at $H = -25$ km. Thick solid lines with filled circles result from 3D model, and dashed lines with open circles result from synthetic profiles for the case of no smearing. In the case of the synthetic profiles, the velocities and contrasts given on the horizontal axes are the values measured from the profiles at $\Delta\lambda_W$ = 280 mÅ corresponding to the average height $\langle H \rangle = -25$ km. In the case of the 3D model, we take the velocities and the temperature variations at the single layer $H = -25$ km of each model grid point.

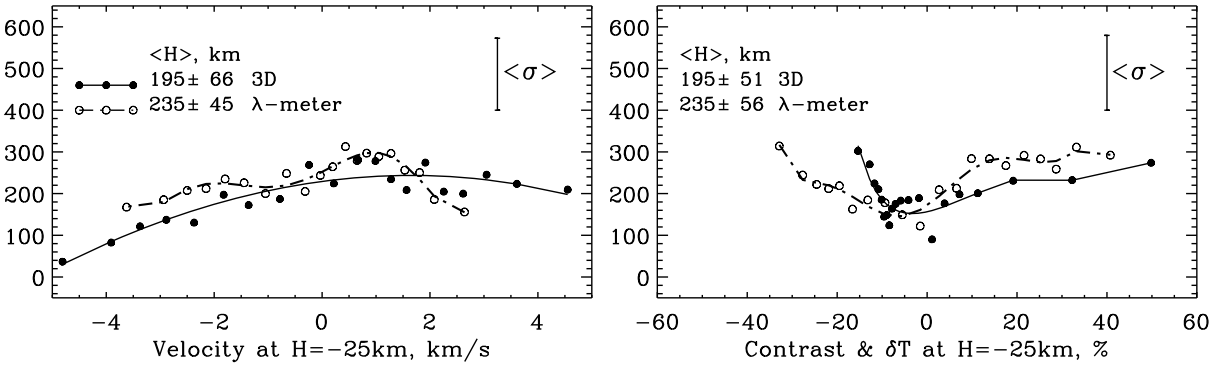

Fig. 12. Height of the contrast sign reversal as a function of the velocity (*left*) and as a function of contrast or temperature variations δT (*right*) at $H = -25$ km. The format of the figure is the same as for Fig. 11.

conditions. To what extent are such dependences sensitive to the degrading effects caused by Earth's atmospheric turbulence? To answer this question, we applied the same analysis to the set of synthetic profile smeared with two values of the Fried's parameters R_0. The results for R_0 = 8 cm (resolution similar to our observations) are shown by open circles with dashed curve in Figs. 8 and 9. The results for R_0 = 38 cm (excellent spatial resolution rarely reached in ground-based observations) are shown by crosses and dotted curve in the same figures. We considered also the case of the profiles with the numerical spatial resolution of the 3D model when the smearing due to seeing and instrumental effects is absent. The latter case is displayed in Figs. 11 and 12 (dash-dotted curves with open circles).

The results obtained with the synthetic profiles clearly demonstrate that the observed dependences are rather sensitive to the seeing conditions. According to Shchukina et al. (2009, Paper I), the spatial smearing reduces the absolute values of the λ-meter velocities, particularly of the strong downward ones.

This explains the difference in the continuum velocity scales on the horizontal axis of Figs. 8, 9, 11, and 12 (left panels) between the cases with $R_0 = 8$, $R_0 = 38$, and the original numerical resolution. In the case with $R_0 = 38$ and in the case of the original resolution, the curves have rather symmetric behavior with respect to the zero velocity point with nearly twice smaller number of the reversal events above the downflowing areas. Under the resolution similar to our observations ($R_0 = 8$ cm), the information on the velocity sign reversal above the downflowing areas is lost. The contrast of granulation also decreases with decreasing the parameter R_0. As a result, all dependences on the granulation contrast become smoother and less pronounced under better seeing conditions. As follows from Figs. 8, 9 and Figs. 11, 12, the average height of the velocity sign reversal increases with improving spatial resolution, whereas the average height of the contrast sign reversal becomes smaller. The difference can reach about 100 km between the case with $R_0 = 8$ cm and the case with original numerical spatial resolution.

The evidence presented above gives us confidence that our results on the velocity and contrast sign reversal are not artifacts caused by specific analysis procedure. Additional evidence is presented in Figs. 11, 12 (solid curves with filled circles). These data illustrate the velocity sign reversal heights and the temperature variation sign reversal heights measured directly from the 3D model snapshot. The temperature variations (δT) are defined relative to the average temperature ($\bar{T}$) over the snapshot at each particular height, i.e. $\delta T = (T - \bar{T})/\bar{T}$. It is clear from the figure that the dependences measured directly from the 3D model are very similar to the ones obtained after spectral synthesis and the λ-meter technique (see dashed-dotted curved with open circles on the same figure). The only remarkable difference is that the λ-meter velocities and contrast values are systematically lower. The latter is easy to understand having in mind that the λ-meter method gives the average information over a certain height range, thus leading to such a reduction.

6. Discussion

The classical picture of the convection breaks in the solar photosphere, starting at least from 50 km above the continuum formation level. The convective elements moving upwards and downwards not only change their sign of contrast but also their direction of motion. Often both events take place at the same time. This process occurs in a wide range of heights up to 650 km. The height where the contrast sign reversal takes places depends strongly on the contrast of granules and intergranules at the continuum formation level. Stodilka (2006) came to the conclusion that the temperature inversion happens in a wide range of heights, from 150 to 500 km. In addition, there is a similar tendency, i.e. the larger the granule, the higher the temperature inversion takes place. According to Puschmann et al. (2005), the temperature inversion occurs for structures with sizes over 1.″5 at heights above 200 km. Our results confirm these conclusions. On the other hand, Stodilka (2006) claims that the temperature reversal events are more often above intergranules, while according to our results, this happen more often above granules (see right panel of Fig. 9). The large scatter in the average height of the contrast (temperature) reversal according to observations of different authors (from 60 to 350 km) not only stems from the observational details (like seeing) and their analysis, but also from the methods used to calculate the formation heights of the observed spectral lines, as correctly pointed out in Puschmann et al. (2005). We think that the main reason for this disagreement

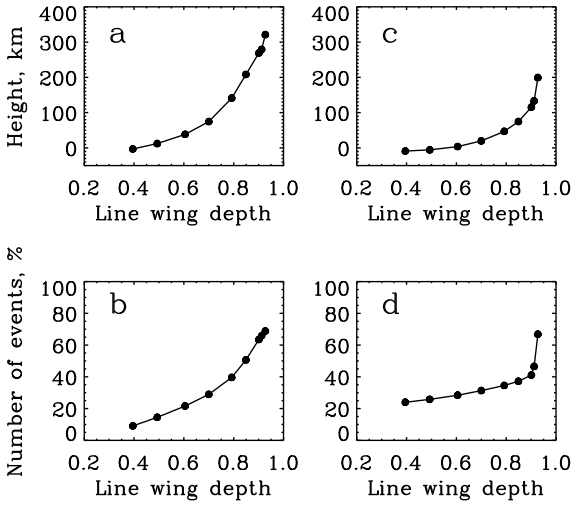

Fig. 13. a) Average height of the contrast sign reversal as a function of Ba II line depth. **b)** Fraction of the events of the contrast sign reversal with height as a function of the Ba II line depth. **c)** and **d)** same for the velocity sign reversal.

is the difference in the formation heights of spectral lines used in different observations. To prove this statement, consider the calculation presented in Fig. 13. The panel *a* of this figure gives the average height of the contrast sign reversal as a function of the Ba II line depth for the our observations. It follows that the larger the line depth, the higher the level of the contrast sign reversal obtained. The panel *b* of Fig. 13 gives the fraction of the contrast sign reversal events as a function of the line depth. As one can see, the stronger lines probe higher atmospheric regions and may, therefore, detect more sign reversals. Since different authors use spectral lines of different strengths (corresponding to different formation heights of the central intensity), it is natural that they obtain different heights of the sign reversal of solar granulation contrast. The panels *c* and *d* of Fig. 13 give similar results but for the heights where the velocity sign reversal takes place. The first authors that pointed out the contrast sign reversal in the solar atmosphere were Evans & Catalano (1972) and Holweger & Kneer (1989). However, not only does the contrast sign reversal take place in the solar atmosphere, but also the reversal of sign of the convective velocities with height. On average, it happens at about 200–300 km high. As far as we know, this property of the convective motions has not ever been studied before.

The comparison of observed dependences with those obtained from the NLTE synthesis of Ba II 4554 Å profiles in the 3D hydrodynamical model of Asplund et al. (2000) have shown that this model reproduces the observed dependences rather well except for the dependence of the height of the contrast sign reversal on the velocity at the bottom layer. We found that all 16 classes of the convective motions are present in the 3D model, and their statistical behavior is similar to the observed. The contrast sign reversal and the velocity sign reversal take place over the whole atmosphere from 50 to 650 km. However, the column structure of granulation is preserved up to 650 km. Almost 40% of all the convective structures detected at the continuum formation height reach 650 km. In particular, 80% of the structures larger than 1500 km in the continuum reach 650 km. Most losses are experienced by the smallest convective elements with sizes below 500 km, while the fraction of the elements with larger sizes increases with height.

7. Conclusions

We performed statistical analysis of the solar granulation velocities and intensities extracted by means of λ-meter technique from the high-resolution observations of the quiet solar disk center in the Ba II 4554 Å line. As this line forms high enough in the atmosphere, it has allowed us to study the properties of granulation at heights not accessed in the earlier studies up to 650 km, i.e. the lower chromosphere. The results of observations were compared with the synthetic data from the 3D hydrodynamical model of the solar convection by Asplund et al. (2000). We found similar dependencies in the observations and simulations smeared to the observational resolution. It gives us confidence in our results and also proves the good quality of the 3D model. Our main findings can be summarized as follows

- About 40% of the column structure of granulation is preserved up to heights around 650 km.
- The average size of granular elements increases with height.
- The granulation can be described by a 16-column model, depending on the sign of contrast and velocity direction at the bottom and top atmospheric levels. All types of motion are found to indeed be present on the Sun.
- The contrast sign reversal of granulation takes place at heights around 200–300 km. At the same heights, on average, the velocity sign reversal also occurs.
- The heights where the sign reversal happens strongly depends on the individual contrast and velocity of granules at the continuum. The larger these parameters, the higher the sign reversal takes place.
- The precise values of the heights of velocity and contrast sign reversal obtained from observations are sensitive to the spatial resolution within their standard deviation error bars.

Acknowledgements. This research was funded by the Spanish Ministerio de Educación y Ciencia through projects AYA2007-63881 and AYA2007-66502 and by the National Academy of Sciences of Ukraine through projects 1.4.6/7-233B and 257Kt.

References

Asplund, M., Nordlund, Å., Trampedach, R., Allende Prieto, C., & Stein, R. F. 2000, A&A, 359, 729
Bendlin, C., & Volkmer, R. 1993, A&A, 278, 601
Brandt, P. 2000, Encyclopedia of Astronomy and Astrophysics, article 2008, Solar Photosphere: Granulation, ed. P. Murdin (Bristol: Institute of Physics Publishing)
Delbouille, L., Neven, L., & Roland, G. 1973, Photometric atlas of the solar spectrum from λ3 000 to λ10 000, Institut d'Astrophysique de l'Université de Liège, Liège, Belgium
Espagnet, O., Muller, R., Roudier, T., et al. 1995, A&AS, 109, 79
Evans, J. W., & Catalano, C. P. 1972, Sol. Phys., 27, 299
Fried, D. L. 1966, Journal of the Optical Society of America (1917–1983), 56, 1372
Holweger, H., & Kneer, F. 1989, in Solar and Stellar Granulation, Proceedings of the 3rd International Workshop of the Astronomical Observatory of Capodimonte, ed. R. J. Rutten, & G. Severino, NATO Advanced Science Institutes (ASI) Series C (Dordrecht: Kluwer), 263, 173
Janssen, K., & Gauzzi, G. 2006, A&A, 450, 365
Khomenko, E., Kostik, R. I., & Shchukina, N. G. 2001, A&A, 369, 660
Khomenko, E., Shelyag, S., Solanki, S. K., & Vögler, A. 2005, A&A, 442, 1059
Kiselman, D. 1994, A&AS, 104, 23
Kneer, F. J., Mattig, W., Nesis, A., & Werner, W. 1980, Sol. Phys., 68, 31
Kostik, R. I., & Khomenko, E. 2007, A&A, 476, 341
Kostyk, R. I., & Shchukina, N. G. 2004, Astron. Rep., 48, N 9, 769
Maltby, P., Avrett, E. H., Carlsson, M., et al. 1986, ApJ, 306, 284
Nordlund, Å, & Dravins, D. 1990, A&A, 228, 155
Olshevsky, V., Shchukina, N. G., & Vasil'eva, I. 2008, Kinematika i Fizika Nebesnich Tel, 24 (3), 198
Puschmann, K. G., Vázquez, M., Bonet, J. A., Ruiz Cobo, B., & Hanslmeier, A. 2003, A&A, 408, 363
Puschmann, K. G., Ruiz Cobo, B., Vázquez, M., Bonet, J. A., & Hanslmeier, A. 2005, A&A, 441, 1157
Ricort, G., Aime, C., Roddier, C., & Borgnino, J. 1981, Sol. Phys., 69, 223
Salucci, G., Bertello, L., Cavallini, F., Ceppatelli, G., & Righini, A. 1994, A&A, 285, 322
Schröter, E. H., Soltau, D., & Wiehr, E. 1985, Vistas in Astronon., 28, 519
Shchukina, N., Olshevsky, V., & Khomenko, E. 2009, A&A, 506, 1393 (Paper I)
Stebbins, R. T., & Goode, P. R. 1987, Sol. Phys., 110, 237
Stein, R. F., & Nordlund, Å. 1998, ApJ, 499, 914
Stodilka, M. 2006, Kinematika i Fizika Nebesnich Tel, 22, N3, 173
Sütterlin, P., Rutten, R. J., & Skomorovsky, V. I. 2001, A&A, 378, 251
Trujillo Bueno, J., & Shchukina, N. 2009, ApJ, 694, 1364